ORIGINAL RESEARCH ARTICLE

Assessment of URANS-Type Turbulent Flow Modeling of a Single Port Submerged Entry Nozzle (SEN) for Thin Slab Continuous Casting (TSC) Process

ALEXANDER VAKHRUSHEV, EBRAHIM KARIMI-SIBAKI, MENGHUAI WU, ANDREAS LUDWIG, GERALD NITZL, YONG TANG, GERNOT HACKL, JOSEF WATZINGER, JAN BOHACEK, and ABDELLAH KHARICHA

The numerical methods based on the unsteady Reynolds-averaged Navier–Stokes (URANS) equations are robust tools to model the turbulent flow for the industrial processes. They allow an acceptable grid resolution along with reasonable calculation time. Herein, the URANS approach is validated against a water model experiment for the special single port submerged entry nozzle (SEN) design used in the thin slab casting (TSC) process. A 1-to-2 under-scaled water model was constructed, including the SEN, mold, and strand Plexiglas segments. Paddle-type sensors were instrumented to measure the submeniscus velocity supported by videorecording of the dye injections to provide both qualitative and quantitative verification of the SEN flow simulations. Two advanced URANS-type models (realizable k–ε and shear stress transport k–ω) were applied to calculate velocity pattern on meshes with various resolutions. An oscillating single jet flow was detected in the experiment, which the URANS simulations initially struggled to reflect. The dimensionless analysis of the mesh properties and corresponding adjustment of the boundary layers inside the SEN allowed to resolve the flow pattern. The performed fast Fourier transform (FFT) verified a good numerical prediction of the flow frequency spectrum. The corresponding simulation strategy is proposed for the industrial CC process using the URANS approach.

https://doi.org/10.1007/s11663-024-03002-8

I. INTRODUCTION

TURBULENT flows, frequently observed in many engineering applications, are of paramount importance. In the continuous casting (CC) process, the molten metal flow becomes very complex especially at the limits of the operational condition.[1–3] It strongly depends on the fresh melt feeding via a submerged entry nozzle (SEN) into the mold cavity. There are so-called ''butterfly effects,'' appearing even at the small flow fluctuations, which can dramatically affect the final product quality, since the melt dynamics in the mold is a footprint of the internal SEN flow.[4] As emphasized by Zhao and Thomas,[2] it is crucial to maintain sufficient amount of the superheat at the top mold level to avoid the ''freezing of the meniscus,'' which might lead to ''hook'' formation and development of the final product surface defects. However, an excessive superheat, in turn, is commonly associated with the internal cracking of the solidified shell and enhanced segregation phenomenon.[5] The proper prediction of the velocity gradient tensor and its invariants assists in analysis of the clogging formation, which dominantly defines melt

ALEXANDER VAKHRUSHEV, EBRAHIM KARIMI-SIBAKI, and ABDELLAH KHARICHA are with the Christian-Doppler Laboratory for Metallurgical Applications of Magnetohydrodynamics, Montantuniversität Leoben, Franz-Josef-Strasse 18, 8700 Leoben, Austria. Contact e-mail: abdellah.kharicha@unileoben.ac.at MENGHUAI WU and ANDREAS LUDWIG are with the Chair of Simulation and Modeling of Metallurgical Processes, Montantuniversität Leoben, Franz-Josef-Strasse 18, 8700 Leoben, Austria. GERALD NITZL is with the RHI Magnesita GmbH, Kranichberggasse 6, 1120 Vienna, Austria. YONG TANG and GERNOT HACKL are with the RHI Magnesita Technology Center, Magnesitstrasse 2, 8700 Leoben, Austria. JOSEF WATZINGER is with the Primetals Technologies Austria GmbH, Turmstrasse 44, 4031 Linz, Austria. JAN BOHACEK is with the Heat Transfer and Fluid Flow Laboratory, Brno University of Technology, 61669 Brno, Czech Republic.
Manuscript submitted November 8, 2023; accepted January 8, 2024.
Article published online February 26, 2024.

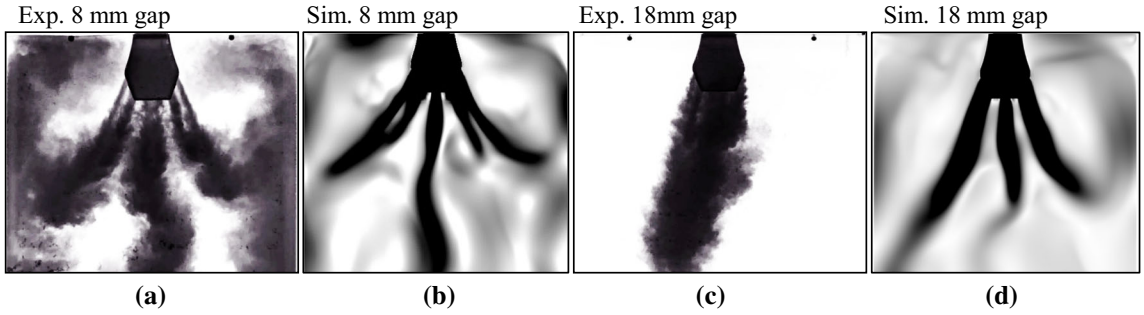

Fig. 1—Water modeling and URANS simulation results (using ''conventional'' numerical grid) for a specific single port SEN design with (*a*) and (*b*) small gap size (8 mm) and (*c*) and (*d*) big gap size (18 mm).

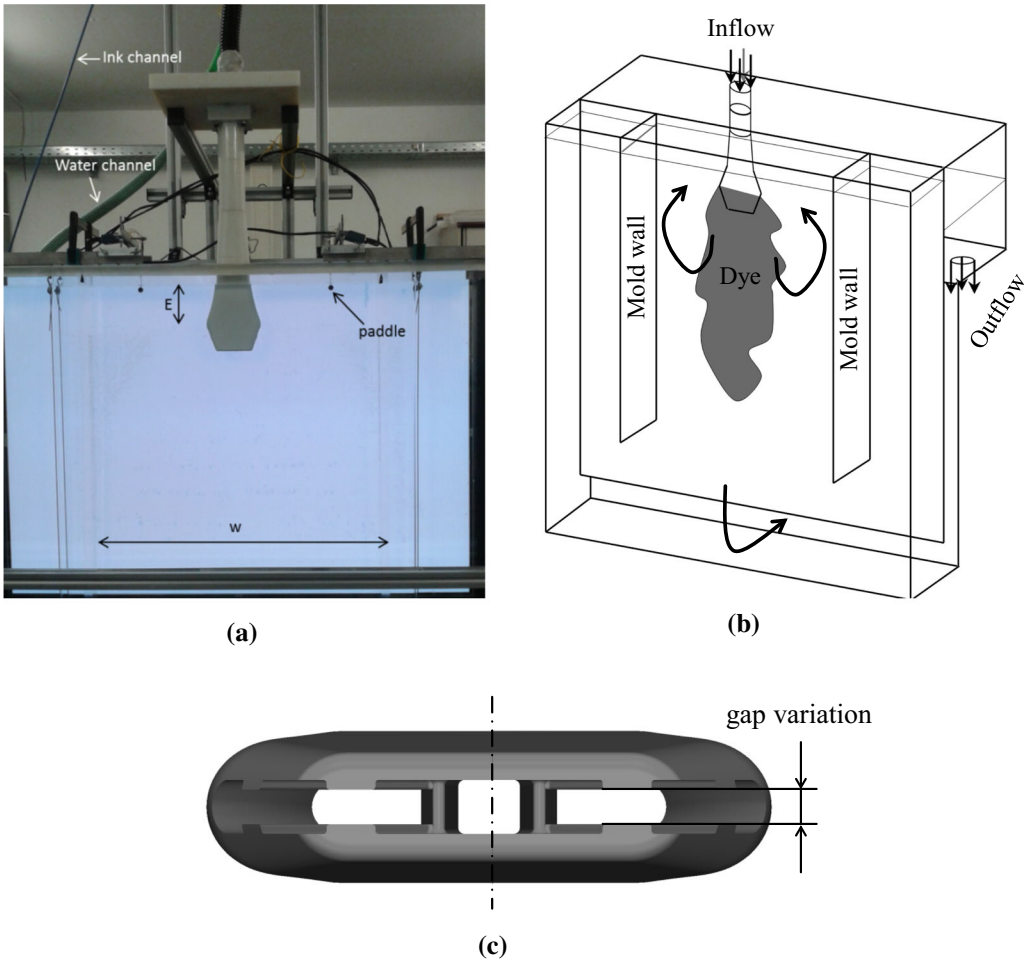

Fig. 2—Water model: (*a*) setup overview; (*b*) flow schematics; (*c*) SEN gap (8 mm, 18 mm).

flow alternation.[6] As pointed out by Barati *et al.*[7–9] and by the current authors,[10] the clogging is often accompanied by parasitic solidification of steel inside the SEN bore, which results in the enhanced meniscus flow and drop in the superheat, both leading to the defects formation.

To reduce the risk of previously described undesired effects, the SEN and mold flow should be carefully optimized. Direct measurements and observations are restricted due to the high temperatures and harsh environment in a casting mill. Thereby, a numerical simulation, employing computational fluid dynamics (CFD), becomes a valuable tool to predict and to avoid the undesired flow scenarios with an aim to establish some recommendations and improvements to the casting process.

Modern CFD software, commercial or open-source (such as OpenFOAM®[11]), allow embedding the sub-models to resolve the smaller levels of the turbulence. Modeling techniques are applied in a wide range,

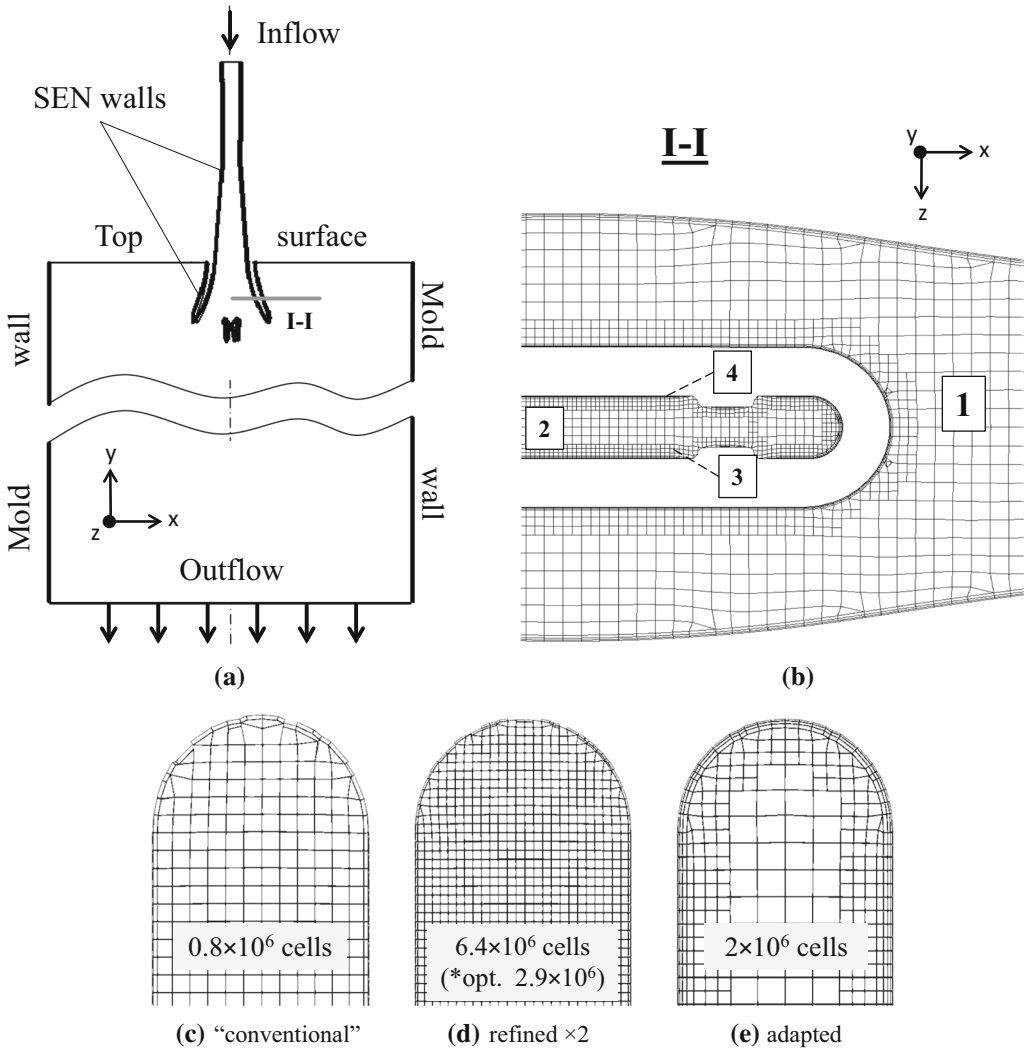

Fig. 3—Simulation domain: (*a*) geometry schematics; (*b*) details of the FVM grid in the horizontal cut I-I with the background mesh (Level 1), cell refinement Levels 2 to 3 and with a wall boundary layer Level 4. Details of the (*c*) "conventional," (*d*) refined by factor 2 and (*e*) adapted meshes inside SEN.

e.g., as a subscale lattice Boltzmann (LB) method,[12] a scale adapting simulations (SAS)[13–16] and, as a last resort, the sophisticated approach of large eddy simulation (LES).[17] Those models use a traditional finite volume method (FVM). However, a meshless approach is more widely applied nowadays to model turbulent flow, solidification, and macrosegregation in the CC process.[18,19] Resolving the turbulent effects is a common task of all turbulence models. As shown previously by the authors,[3,20,21] a proper turbulent flow calculation plays a dramatic role on calculated solidification profile. However, the complex techniques of a high order (*e.g.*, LES) are computationally expensive.[22] Thus, the Reynolds-averaged Navier–Stokes equations (RANS), more precisely the unsteady-RANS, remain to be the most applicable approach for engineering tasks.

Over the past decades, numerical simulation has been commonly fitted to engineering applications in the casting industry by iteratively increasing computational element number to achieve mesh-independent convergence. That leads to a drastic growth of the computational time, requiring weeks and months to complete a single study on the industrial scale. Alternative techniques do not restrict the mesh quality and aim for fast and acceptable qualitative results. Some complex phenomena (*e.g.*, turbulent flow) are, thus, ignored as a reckoning for the lack of accuracy. An intermediate and mostly applied approach consists of keeping a coarse mesh in the core of the liquid bulk and introducing a special near-wall treatment by employing semi-empirical relations such as wall functions. They are obtained from the experimental work or by performing the direct numerical simulations (DNS).[23]

Previously authors presented the experimental and corresponding numerical studies for the free-surface slag flow in the CC mold[24] as well as for the non-metallic inclusions motion in a CC tundish under the strong turbulence.[25] The pressure drop effects, detailed for the stopper region in Javurek *et al.*,[26] were supplemented by the recent investigations of Thumfart *et al.*[27] considering the purging gas influence on the melt flow asymmetry and instability inside the SEN.

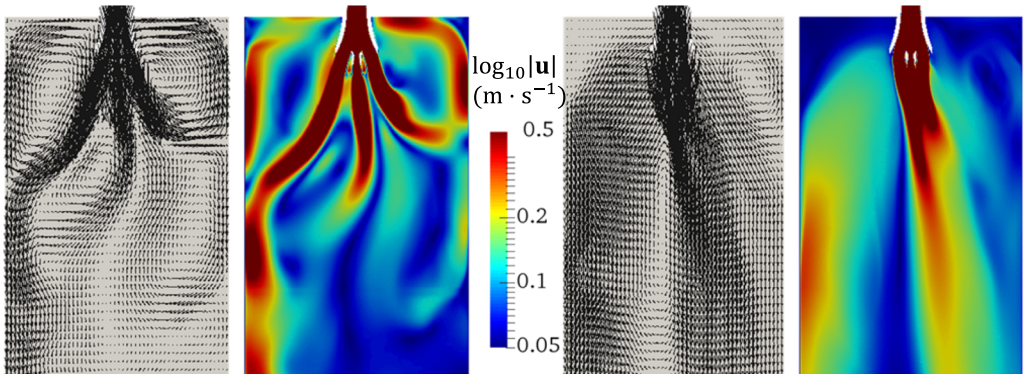

Fig. 4—Simulation results for (*a*) "conventional" grid (0.8×10^6 cells); (*b*) refined by factor of 2 (6.4×10^6 cells) and adapted grid (2×10^6 cells).

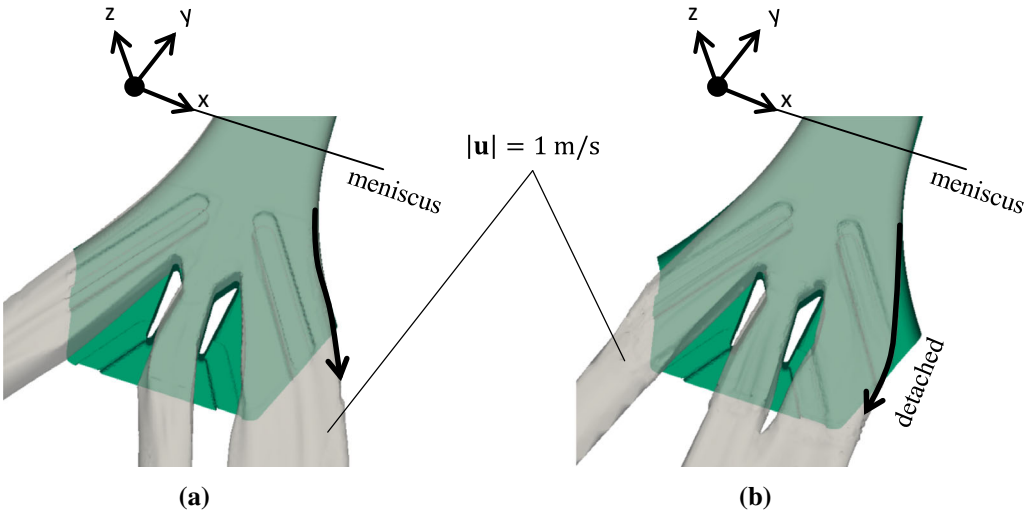

Fig. 5—Simulated flow pattern inside the SEN with (*a*) unresolved and (*b*) resolved detachment.

The current study employs a water model experiment, performed by RHI Magnesita GmbH (Austria), for the modern thin slab casting (TSC) technology, which is characterized by high casting speeds and special SEN designs.[28] The classical double roll pattern in experiment (Figure 1(a)) was accurately matched by the URANS calculations (Figure 1(b)) on a "conventional" numerical mesh, which was assembled according to a mesh convergence criterion based on the authors' long time experience in this field. The details of the mesh design process are disclosed later in this study. However, for a specific regime with an oscillating jet (Figure 1(c)), the numerical model was unable to predict the flow pattern (Figure 1(d)). The size and basic refinement of the mesh were specified by two different TSC geometries with the SEN gap of 8 and 18 mm. The instable, asymmetrical, and/or periodical flow in a funnel TSC mold is known from a number of published studies both experimental and numerical,[29–31] which can later affect the flow behavior under applied magnetic field.[32,33] A discrepancy between modeling and experiment in Figure 1 gave a motivation for the current study, aiming to evaluate the URANS simulation techniques to correctly predict the real SEN flow including the mold region of the continuous caster when a featured behavior is detected.

We show a verification example of the SEN flow in a TSC mold using URANS-type simulation based on the water modeling and corresponding FFT analysis. Based on the performed studies, the modeling strategy was adjusted to resolve initial mismatch with the experimental measurements. The results of the presented work have general importance for engineering applications of CFD for the CC process involving a turbulent flow.

II. WATER MODELING EXPERIMENT

The experiment setup for the thin slab CC is shown in Figure 2. The mold is made of transparent Plexiglas. The geometry of the water model is 1-to-2 under scaled to the real size of a thin slab caster (Table I). A special SEN, named as UFM single port SEN by the producer (RHI Magnesita GmbH), is prepared with a 3D printing

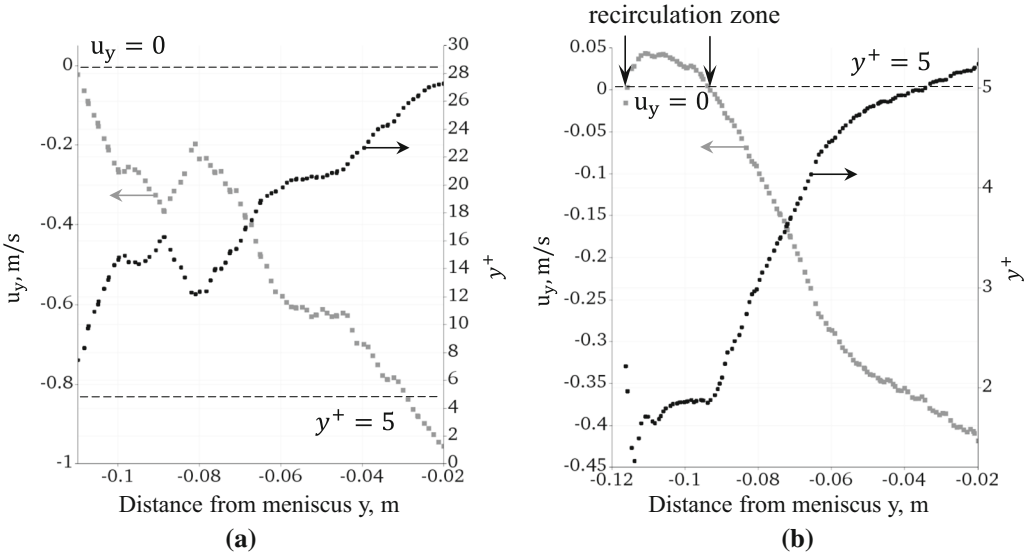

Fig. 6—Distribution of the vertical velocity component u_y and y^+ function along the detachment zone for the (*a*) "conventional" and (*b*) refined meshes.

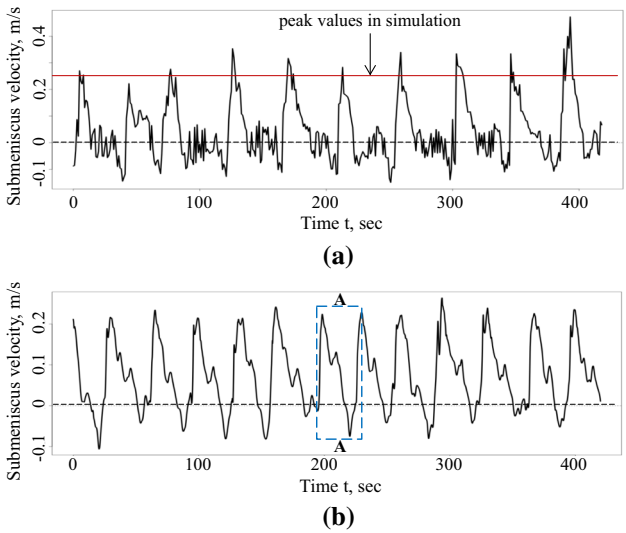

Fig. 7—Comparison of the submeniscus flow velocities at the positions of paddle sensors: (*a*) in the water experiment; (*b*) in the simulation.

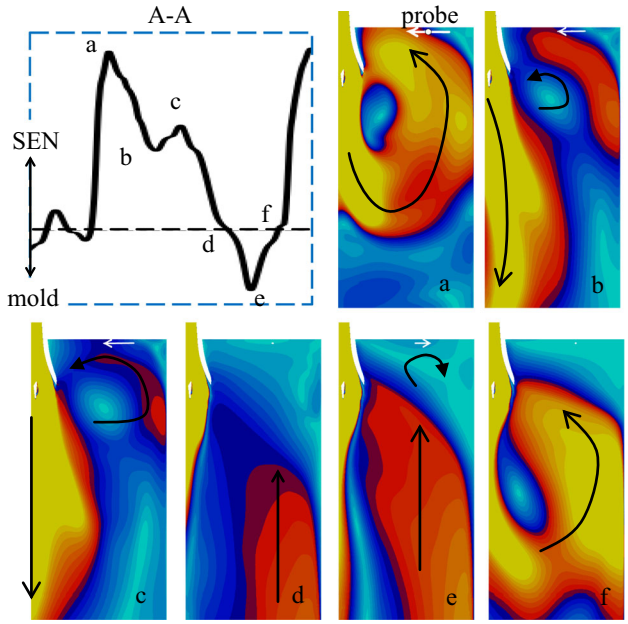

Fig. 8—Detailed view of the flow pattern within a single period of the jet oscillation (a dashed window marked as 'A-A' in Fig. 7(b)).

technique. The inner gap size of the SEN (Figure 2(c)) is varied for different experimental trials. A dye injection is made through the inlet above the SEN, and a high-resolution camera with a frequency of 15 to 18 frames per second is implemented in front of the wide face to capture the flow pattern in the CC mold. Additionally, two paddle sensors of a ball shape ($\emptyset = 5$mm) are positioned 10 mm under the water surface (on the left and right side of the SEN) to measure the submeniscus velocity of the flow for duration of 30 minutes with a frequency of 10 Hz. All recorded data were visualized and post-processed using an in-house software package.

A volumetric flow is determined by dynamic similarity between the water model and an industrial process according to the Froude criterion:[34–36]

$$Q_m = \left(\frac{1}{k_m}\right)^{2.5} \times Q_r, \qquad [1]$$

where Q_m is the water model flow rate; Q_r is a corresponding flow rate of the real casting process; and k_m is the model scaling factor (here equal to 2). Based on the Eq. [1], a casting speed in the water model is calculated as follows:

$$u_m = \sqrt{\frac{1}{k_m}} \times u_r. \qquad [2]$$

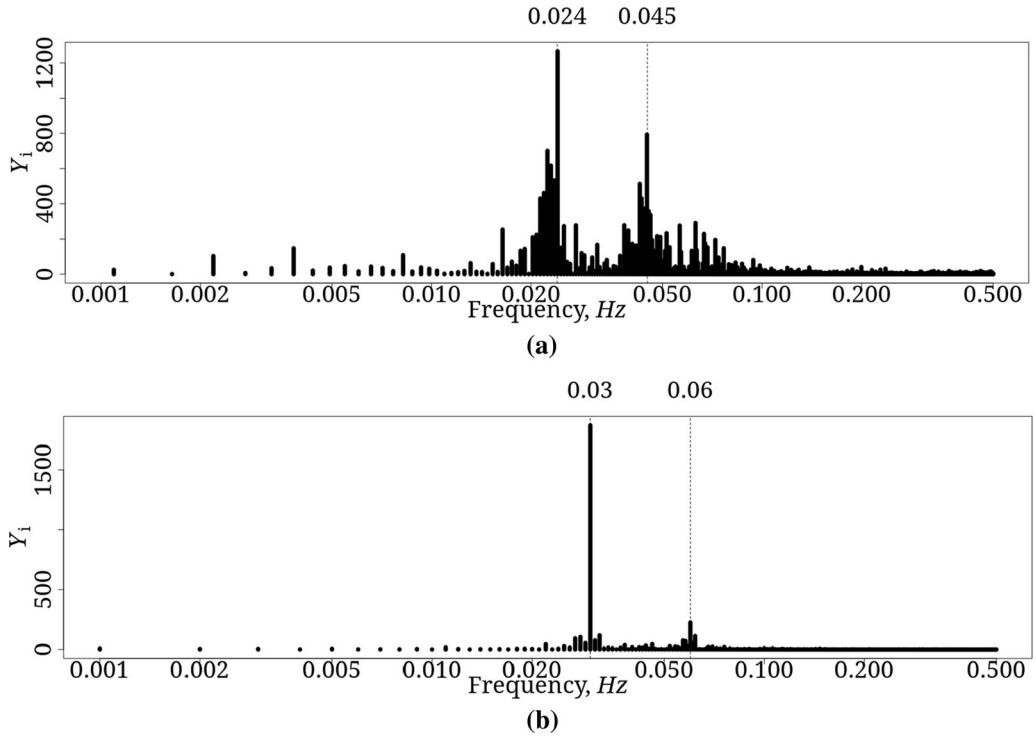

Fig. 9—Fast Fourier transform (FFT) for (*a*) experimental and (*b*) simulated data; frequency axis is in logarithmic scale.

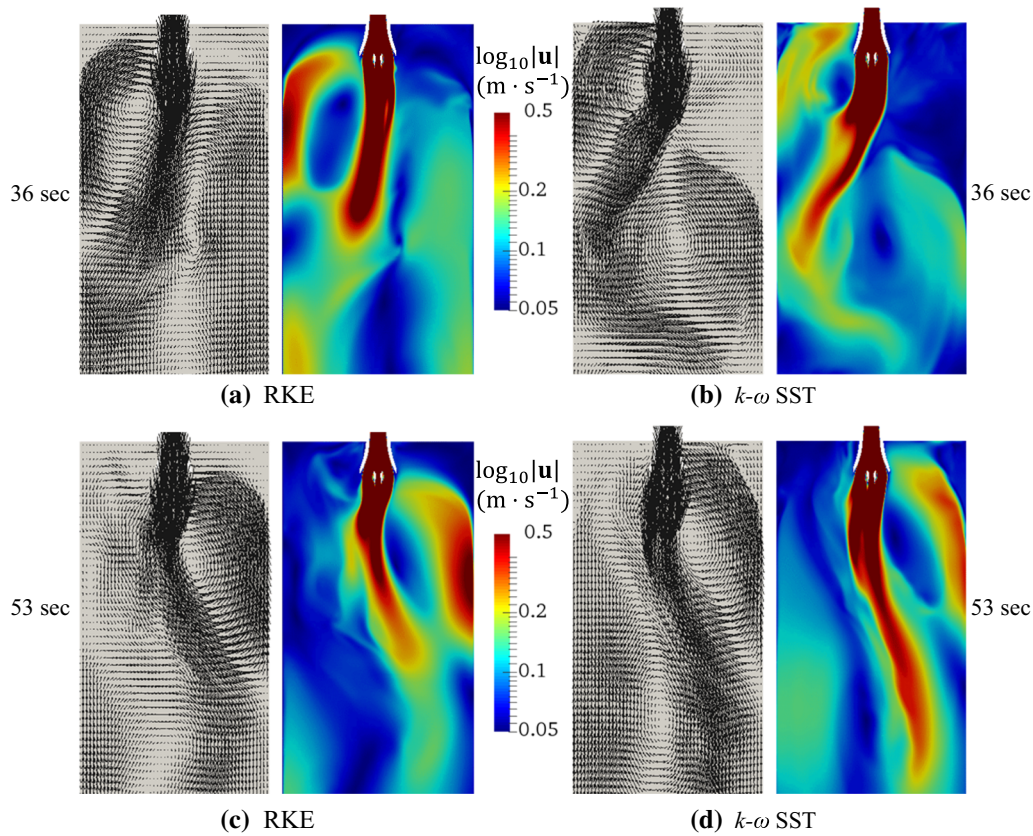

Fig. 10—Vector and contour fields of velocity **u** simulated with RKE and *k*–*ω* SST models at (*a*) and (*b*) 36 seconds and (*c*) and (*d*) 53 seconds of the simulated physical time.

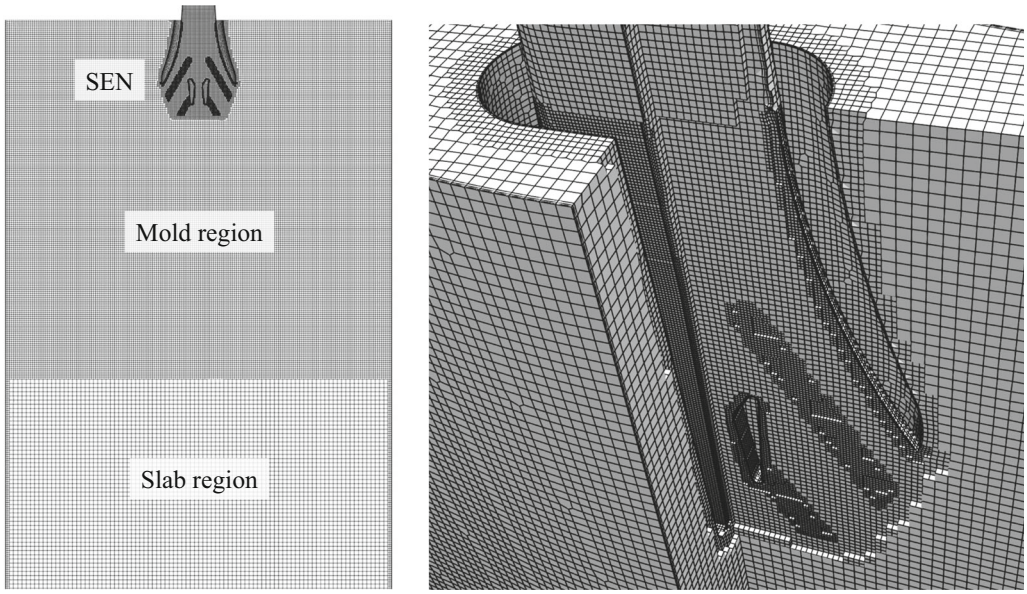

Fig. 11—Designed mesh for the TSC process modeling using URANS approach: (*a*) midplane cut of the adapted grid for the SEN, mold, and slab regions; (*b*) mesh refinement details inside the SEN.

Table I. Casting Parameters for the Real Industrial Process and for the 1-to-2 Scaled Water Model

Data Set	Slab Width (mm)	Slab Thickness (mm)	Casting Speed (m/min)
Real Process	1400	112.5	3.4
Water Modeling	700	56.25	2.4

Table II. Settings of the Numerical Model and Material Properties

Turbulence Model Parameters	Realizable k–ε: $\mathrm{Pr}_{t,k} = 1$, $\mathrm{Pr}_{t,\varepsilon} = 1.2$, $C_{2\varepsilon} = 1.9$. SST k–ω: $\mathrm{Pr}_{t,k1}=0.85$, $\mathrm{Pr}_{t,k2}=1$,$\mathrm{Pr}_{t,\omega1}=0.5$,$\mathrm{Pr}_{t,\omega2}=0.856$,$\alpha_1=5/9$, $\alpha_2=0.44$, $\beta_1 = 0.075$, $\beta_2 = 0.0828$, $\beta^* = 0.09$, $a_1 = 0.31$, $b_1 = 1$.
Wall Treatment	standard k, ε, ω wall functions (see Table IV).
Pressure-Velocity Coupling	PIMPLE, Gauss-Green discretization of gradients
Flow Time and Space Discretization	transient 1st order Euler, 2nd order CD/UW blending.
Water Density	998.2 kg m^{-3}
Water Kinematic Viscosity	1.0048 10^{-6} m^2 s^{-1}

The casting parameters and the mold dimensions, considering both the real casting and water model, are summarized in Table I.

Before each experimental trial, the mold region is filled with clean water. The experiment starts to run for 10 min until a stable flow is achieved. After the initial stage, the paddle sensors start to record the submeniscus velocity. The dye was injected from the SEN inlet for 6 seconds. The high-resolution video camera recordings were taken for 30 seconds to analyze the flow pattern in the mold. Notice that, for each setting of the CC and SEN design, 5 trials were made to ensure the repeatability of the result. The experimental recordings can be found in the Supplementary Video S1.

III. NUMERICAL MODEL

All symbols used hereinafter are listed in the Nomenclature. A special emphasis in the current study is made on the RANS (particularly URANS) approach, which has been proven to be a reliable and effective computational method for engineering applications like continuous casting. The governing equations for the incompressible turbulent flow are as follows:

$$\nabla \cdot \mathbf{u} = 0, \qquad [3]$$

$$\rho \frac{\partial \mathbf{u}}{\partial t} + \rho \nabla \cdot (\mathbf{u} \otimes \mathbf{u}) = \nabla (2\mu_{\mathrm{eff}} \mathrm{dev}(\dot{\boldsymbol{\varepsilon}})) - \nabla p, \qquad [4]$$

defining the effective dynamic viscosity as a sum of the molecular and the turbulent ones $\mu_{\text{eff}} = \mu_\ell + \mu_t$; the rate-of-strain tensor is a symmetric part of the velocity gradient tensor:

$$\dot{\boldsymbol{\varepsilon}} = \text{Sym } (\nabla \mathbf{u}) = \frac{1}{2}\left(\nabla \mathbf{u} + (\nabla \mathbf{u})^{\text{T}}\right). \quad [5]$$

For the closure of the model equation system Eqs. [3] through [5], a RANS approach was employed for the turbulence, based on the realizable k–ε (RKE) model.[37] The RKE provides improved performance for flow calculations involving boundary layers under strong pressure gradients, strong streamline curvature involving rapid strain, moderate swirl, and locally transitional flows (*e.g.*, boundary layer separation). It overcomes the limitations of standard k–ε model, which is not presented in this study due to its poor performance on complex flows. The following transport equations for the turbulence kinetic energy and dissipation rate were

$$\frac{\partial(\rho k)}{\partial t} + \nabla \cdot (\rho \mathbf{u} k) = \nabla \cdot \left(\left(\mu_\ell + \frac{\mu_t}{\text{Pr}_{t,k}}\right)\nabla k\right) + \rho G - \rho \varepsilon, \quad [6]$$

$$\frac{\partial(\rho \varepsilon)}{\partial t} + \nabla \cdot (\rho \mathbf{u} \varepsilon) = \nabla \cdot \left(\left(\mu_\ell + \frac{\mu_t}{\text{Pr}_{t,\varepsilon}}\right)\nabla \varepsilon\right) + \rho C_{1\varepsilon}\|\mathbf{S}\|\varepsilon - \rho C_{2\varepsilon}\frac{\varepsilon^2}{k + \sqrt{\frac{\mu_\ell}{\rho}}\varepsilon}, \quad [7]$$

Table III. Boundary Conditions

Boundaries (Labelled in Fig. 3(a))	Boundary Condition Type
Inflow	pressure inlet
Outflow	(i) normal component: water outflow rate of 5.67 m^3/h (ii) tangential component: free slip (no shear)
Top Water Surface	free slip (no shear)
Mold and SEN Walls	no slip wall

where $\mathbf{S} = \text{dev } \dot{\boldsymbol{\varepsilon}}$ is the strain-rate tensor. The turbulent viscosity and the production term for the turbulent kinetic energy are given by

$$\mu_t = \rho C_\mu \frac{k^2}{\varepsilon}, \quad [8]$$

$$G = 2\mu_t \|\mathbf{S}\|^2, \quad [9]$$

where $C_{1\varepsilon}$ and C_μ are functions of velocity gradient to ensure positive Reynolds normal stresses.

The shear stress transport (SST) k–ω model is used as a second URANS turbulence model in the presented study, introduced by Menter.[38] The k–ω SST is superior to k–ε type models by applying a gradual transition from the near-wall into core region of flow and by limiting the turbulence viscosity by introduction of the corresponding blending functions. The closure equations for k and ω, used in the OpenFOAM® FVM framework, are based on the updated version from Menter *et al.*[39]:

$$\frac{\partial(\rho k)}{\partial t} + \nabla \cdot (\rho \mathbf{u} k) = \nabla \cdot \left(\left(\mu_\ell + \frac{\mu_t}{\text{Pr}_{t,k}}\right)\nabla k\right) + \rho G - \rho \beta^* \omega k, \quad [10]$$

$$\frac{\partial(\rho \omega)}{\partial t} + \nabla \cdot (\rho \mathbf{u} \omega) = \nabla \cdot \left(\left(\mu_\ell + \frac{\mu_t}{\text{Pr}_{t,\omega}}\right)\nabla \omega\right) + \alpha\rho\|\mathbf{S}\|^2 - \beta\rho\omega^2 - (F_1 - 1)\rho \text{CD}_{k\omega}, \quad [11]$$

where the cross-diffusion term $\text{CD}_{k\omega}$ is multiplied by a switching function F_1, which controls the behavior from the wall region into a freestream. Further parameters of the model are blended in such a manner that $f = F_1(f_1 - f_2) + f_2$ where $f = \text{Pr}_{t,k}, \text{Pr}_{t,\omega}, \alpha, \beta$ (see Table II for parameters variation). The calculation of the turbulent viscosity is enhanced in the k–ω SST model as following:

$$\mu_t = \rho \frac{a_1 k}{\max(a_1 \omega,\ b_1 F_2 \|\mathbf{S}\|)}, \quad [12]$$

where the second blending function F_2 plays a role of the shear stress limiter.

Table IV. Wall Functions (von Karman Constant $\kappa = 0.41$; Coefficient $E = 9.8$)

Name in OpenFOAM® CFD package	Corresponding Wall Law Equation in (i) Viscous ($y^+ < y^+_{\text{lam}}$) and (ii) Logarithmic Boundary Layer ($y^+ > y^+_{\text{lam}}$)
nutkWallFunction	(i) $\mu_t = 0$; (ii) $\mu_t = \mu_\ell\left(\frac{y^+\kappa}{\ln(Ey^+)} - 1\right)$.
kqRWallFunction	a wrapper for the zero-gradient condition normal to the wall: (i) to (ii) $\mathbf{n} \cdot \nabla k = 0$.
epsilonWallFunction	(i) $\varepsilon = 2k\frac{\mu_\ell}{\rho \Delta_\perp^2}$; (ii) $\varepsilon = C_\mu k^{3/2}\frac{\rho}{\mu_t \Delta}$.
omegaWallFunction	(i) $\omega = 6\frac{\mu_\ell}{\rho \beta_1 \Delta^2}$; (ii) $\omega = \sqrt{k}\Big/C_\mu \kappa \Delta$.

The simulations were performed using open-source CFD package OpenFOAM®.[11] A collocated non-staggered variable arrangement was used for the Finite Volume Method (FVM)[40] to solve the governing equations. The Rhie–Chow interpolation[41] was applied to decouple the cell-centered calculation of pressure and velocity fields, which commonly results as chequerboard oscillations in the pressure-base numerical algorithms.

The simulation domain overlay with the geometry schematics including SEN and funnel-type TSC mold is found in Figure 3(a). The details of the general numerical grid structure, aiming to increase the calculation accuracy, while keeping a reasonable calculation time, are shown in Figure 3(b). The coarse cells (Level 1) are used in the core of the flow inside the mold cavity, whereas inside the SEN two-level mesh refinements (stages 2 and 3) are done supplemented by the introduction of the wall boundary layer as Level 4.

Different investigated mesh types are shown in Figures 3(c) through (e), namely "conventional," refined by factor of 2 and adapted grid. Hereinafter, a "conventional" TSC mesh (as in Figure 3(c)) is defined to follow a set of rules: (i) the narrow dimensions of domain (*e.g.*, mold thickness) are resolved by 15 to 20 cell layers in the core region at Level 1; (ii) a first refinement Level 2 is applied around the SEN with an additional refinement Level 3 inside the SEN; (iii) a wall boundary layer is introduced consisting of the prismatic finite volume elements. As a note, the transition between consequent refinement levels consists of 3 cell layers. The presented criteria for the "conventional" mesh are the results of a long sequence of the mesh convergence studies and consistent two-decades knowledge of the current authors in the field of the TSC process modeling.

Two other mesh types, the refined by factor of 2 in Figure 3(d) and adapted grid in Figure 3(e), which was developed during the presented investigation, are discussed in Section IV–A considering the corresponding performance and accuracy of the numerical solution.

The simulation settings (time and space discretization schemes, turbulence model parameters), fluid properties, and boundary conditions (BC) for the simulation domain (Figure 3(a)) are summarized in Tables II and III. In the present study, we applied a velocity outlet BC of a special type, the so-called *fixedNormalSlip* BC in the OpenFOAM® package. Hereafter, the normal velocity component is defined by the constant outflow rate. That cancels a backflow development, which is highly expected for the oscillating jet. The backflows cause an unphysical velocity growth at the outlet and result in the simulation crash. Along the tangential direction, a free slip is applied. Thus, the oscillating jet and vortex structures are allowed to travel transversally. The pressure inlet serves as a reliable tool for generating a natural inlet velocity profile. Based on our experience, such a technique is recommended for the CC modeling as a one-step-ahead of the traditional velocity inlet / pressure outlet approach.

To reduce the computational cost, a special PIMPLE[42] algorithm is applied being a blending of the Patankar's semi-implicit method for pressure-linked equations (SIMPLE)[43] and Issa's pressure implicit with splitting of operator (PISO)[44] algorithms. It provides stability and accuracy of the numerical solution for CFL numbers > 1 and allows increasing a time step.

Since the resolution of the viscous sublayer in vicinity of the wall becomes computationally challenging for engineering applications, the wall functions approach was used for the simulation of the turbulent flow as listed in Table IV.

Boundary of the viscous sublayer y^+_{lam} in the model is calculated from a non-linear equation for the intersection of the viscous and logarithmic law-of-wall:[45,46]

$$y^+_{\text{lam}} = \frac{1}{\kappa}\ln\left(\max\left(E\, y^+_{\text{lam}},\ 1\right)\right). \qquad [13]$$

For reference, the boundary condition for ε and ω provides a wall constraint for these variables, and the turbulent kinetic energy production G for low- and high-Reynolds number turbulence models.

IV. RESULTS AND DISCUSSIONS

Corresponding to a mismatch between the experiment, displayed in Figure 1(c), and modeling (Figure 1(d)), the SEN with a big gap size (18 mm) was considered in further studies to disclose the origins of the discrepancies.

A. *Mesh Resolution Studies*

The results of the numerical simulation on different meshes are shown in Figure 4. The flow pattern is presented as a vector field and velocity magnitude distribution. On a "conventional" grid with 0.8×10^6 cells (Figure 3(c)), the numerical simulation has predicted a multi-jet flow (Figure 4(a)), which totally diverges from the experimental observations (Figure 1(c)). However, the numerical results for the refined by factor 2 mesh (see Figure 3(d)) with 6.4×10^6 cells matched with the experiment by reflecting a single jet swinging between the narrow walls of the TSC mold (Figure 4(b)).

A 3D flow pattern inside the SEN is rendered in Figure 5. A cut-section through the nozzle's interior is represented in green color; a semitransparent iso-surface corresponds to velocity magnitude of 1 m/s.

According to the flow structure inside the SEN (Figure 5(a)), there is no detachment observed using "conventional" mesh. In the case of the finer grid, a single jet behavior is resolved (Figure 5(b)). Thus, the introduction of the cell refinement, which additionally led to a finer wall layer in Level 4, resulted in a correct prediction of the complex flow pattern including the separation phenomenon. However, the grid size grew drastically. Corresponding CPU time exceeded reasonable limits for the similar TSC simulations using URANS. As follows, a detailed analysis of the wall meshes is performed with the goal of establishing the guidelines for the URANS simulations with application to continuous casting.

Quantitatively, the mesh property at the wall can be described by a so-called y-plus factor as estimated from the friction velocity u_τ and the distance from the wall Δ:

$$y^+ = \frac{\rho u_\tau \Delta}{\mu_\ell}, \quad [14]$$

where for the RANS approach the friction velocity u_τ is calculated using

$$u_\tau = (C_\mu)^{1/4} \sqrt{k}. \quad [15]$$

Theoretically, the turbulent boundary layer consists of a viscous ($y^+ < 5$), transition ($5 < y^+ < 30$) and fully turbulent ($y^+ > 30$) regions.[47] Considering that, we analyze (i) y^+ distribution in the presented cases; (ii) summarize the origins of a poor model performance on "conventional" grid; (iii) provide guidelines for FVM mesh construction to meet quality and performance criteria.

A vertical velocity component u_y and the y^+ function are plotted in Figure 6 along the side-line of the internal SEN wall at the detachment zone, marked with the black arrow in Figure 5. As shown in Figure 6(a) for the "conventional" mesh, the y^+ values mostly fall into a transition region of velocity boundary layer. However, by refining the boundary layer mesh (Figure 6(b)), the calculated y^+ is mostly smaller than 5 and shifts into a viscous sublayer. A recirculation zone occurs between 100 and 120 mm below the meniscus (Figure 6(b)), which indicates the occurrence of the flow detachment.

These results showed the critical importance of wall mesh size estimations, especially to capture flow separation. Therefore, the applied wall functions approach performs poorly in the critical areas of the turbulent flow considering URANS if the near-wall mesh elements are in the buffer region. On the contrary, the simulation correctly reflects the separation phenomenon when the mesh quality is enhanced to resolve the viscous sublayer. That explains why the experimental double roll pattern was correctly modeled by URANS for the 8 mm gap SEN using wall functions and struggled for 18 mm gap SEN with the featured single jet phenomenon.

Next, the numerical grid was optimized by restricting the refinement zone to the SEN region. As a first iteration result, the mesh size was decreased from 6.4×10^6 to the marked with "*" in Figure 3(d) 2.9×10^6 cells. The SEN grid structure remained the same (Figure 3(d)) consistently capturing the single jet behavior (Figure 4(b)).

Finally, an adapted mesh was assembled (see Figure 3(e)) consisting of 2×10^6 elements including coarser cells of Level 2 in the core region, Level 3 near the SEN wall and accurately resolved viscous sublayer at Level 4. Overall 3D structure of the adapted grid and the details of the near wall refinement are detailed in the later Section IV–C.

B. *Numerical Model Verification*

After the qualitative agreement with the experiment was achieved, the accuracy of the numerical model was investigated using adapted mesh. The usage of a different RANS model (see later discussions for the k–ω SST modeling) did not change the results significantly neither qualitatively nor quantitatively.

Consequently, the data sampled by the paddle sensors (Figure 2(a)) were used as a reference for the corresponding values, collected from the exact same locations in the simulation domain.

The measured and simulated submeniscus velocities are compared in Figure 7. Positive velocities correspond for the flow motion toward the SEN, the negative values indicate that the flow is diverging from the SEN toward the mold narrow wall.

For the studied time interval, 10 periods were detected in the experiment for the flow toward the SEN, whereas the simulation predicted 12.5. Moreover, the maximum submeniscus velocity was slightly underpredicted. However, a very good match was achieved for the flow from SEN toward mold walls (negative submeniscus velocity). Additionally, in the experiment, a high frequency noise is observed at the transition point between two flow regimes, which is significantly smoothed by URANS simulation. It possibly originates from the physical outlet that could produce some flow instabilities by its design.

To explain the complex flow behavior, a single jet oscillation period, marked with the 'A-A' window in Figure 7(b), is analyzed as shown in Figure 8. It was found that a peak submeniscus velocity (point **a**) corresponds to the time instance when the jet turns completely to one narrow side of the mold. During the next period (section **a–b** of the curve), velocity magnitude decreases, while the jet is pointed almost downwards. Sequentially, a submeniscus vortex is developed, responsible for the slight velocity increase at the segment **b-c**. When the jet completely bends toward the opposite mold narrow wall, a stagnation zone is formed (point **d**) followed by the strong back flow coming upwards and forming an opposite vortex at moment **e**. Such a flow behavior explains a negative peak **d–e–f**, which is smaller by amplitude than a positive one. In turn, at moment **f** the opposite vortex is damped by the mean jet, which oscillates backwards. The whole analyzed cycle of the jet motion repeats with relatively constant frequency and amplitude. For a detailed picture the readers are highly advised to refer to the Supplementary Video S2 for a clear understanding of the flow dynamics.

For more detailed analysis, a fast Fourier transform (FFT)[48] was calculated both for the experiment and simulation (Figure 9). It converts measured velocities in Figure 7 to their representation in the frequency domain. The samples, measured during 30 minutes with the frequency of 10 Hz, are transformed into the FFT sequence consisting of 18000 complex numbers. Only the first half (9000) of FFT is used, since the second half is its mirrored copy.[48] All elements correspond to equally spaced frequencies between 0 and 5 Hz (half of the original one). The initial signal (see Figure 7) can be represented as a combination of sinusoids with the calculated frequencies and amplitudes from the FFT data.

Next, FFT is normalized using a 'time-integral squared amplitude' definition of the input signal power:

$$Y_i = \Delta t^2 \cdot |H_i|^2 \quad [16]$$

where H_i are the complex FFT values described previously; Y_i represent the real values of the normalized FFT output. The normalization by Eq. [16] is helpful for amplifying the peaks in the FFT plots. As one can see from Figure 9, two dominant frequencies are found both in the experiment and simulation. They correspond to the period of the main jet oscillations and to the small submeniscus vortex formation.

The main jet oscillation frequency was found to be 0.024 Hz which corresponds to the period of 41.7 seconds compared to 0.03 Hz and 33.3 seconds in the simulation. That difference gives exactly the ratio of 1.25 which was detected previously in Figure 8. It should be mentioned, that for the submeniscus vortex, we observed frequency of 0.045 Hz (period of 22.2 seconds) in the water modeling and 0.06 Hz (16.7 seconds) for the numerical simulation. It can be concluded, for the smaller structures, we get a slightly higher mismatch of 1.33 for the frequencies. It is also obvious from the FFT plot in Figure 9 that we obtain the same order of the amplitude for the main jet oscillations, but significantly undershoot the submeniscus recirculation zone. This can be partially explained by the high numerical diffusivity of the employed URANS approach and exclusion of the free-surface motion in the presented study.

Next, the comparison of the numerical results obtained both with RKE and k–ω SST turbulence models using the adapted mesh is presented in Figure 10. Velocity distribution (vector field and magnitude contour-plots) is shown at two representative instances of the simulated physical time, namely 36 and 53 seconds. The k–ω SST revealed less diffusive behavior than the RKE model: more complex vortical structures and a developed flow pattern were obtained in comparison to the RKE case. However, the main frequencies, derived from the FFT analysis for both models, remained the same. Therefore, it is possible to employ both models, which are known to be sophisticated among the RANS family approaches. However, the k–ω SST is noticeably computational-demanding as a trade-off for more elaborated treatment of the turbulent effects. The dynamic of the results presented in Figure 10 is detailed in Supplementary Video S3.

C. *Suggested Strategy for the URANS Simulations in CC*

Since the URANS simulations represent an effective tool for the TSC modeling, a corresponding adaptive numerical grid must be constructed, supporting the calculation efficiency.

The overall suggested mesh structure is presented in Figure 11(a). It consists of the SEN region, continuous casting mold cavity and possibly includes the slab part depending on the scope of a numerical study. Each region has its specific refinement level. We kindly refer the readers to the "conventional" mesh definition given in the current manuscript. Additionally, as seen in Figure 11(a), the cells can be coarsened in the lower regions. That can be performed in all directions in a pure hydrodynamical case, or streamwise only. The latter is valid if the heat transfer is included since the dominant temperature gradients (to be resolved) are typically normal to the slab walls.

Close to the SEN, a further refinement is applied to capture the inner bore gaps and the refractory walls curvature as displayed in Figure 11(b). An additional level is introduced for the geometry features such as grooves and ledges. Finally, the prismatic layers are inflated along the walls.

The near-wall cells must be kept inside the logarithmic region of the turbulent boundary layer for common flow types, where the classical CC flow pattern is expected. Accordingly, the wall functions approach should be applied.

However, if a featured flow behavior is expected inside the SEN, such as flow separation discussed in this paper, further analysis for the wall boundary layer must be performed, detailed next in this section.

Based on the results of the presented studies, the initial wall mesh estimation can be performed using the skin friction coefficient from Schlichting *et al.*[46] to estimate near-wall control volume centroid. The calculations start with a Reynolds number estimation:

$$\mathrm{Re} = \rho U_0 L_0 / \mu, \qquad [17]$$

where U_0 and L_0 are the characteristic freestream velocity and geometry length scale. An empirical correlation for the skin friction coefficient in a fully developed turbulent flow with $\mathrm{Re} < 10^9$ is:[46]

$$C_\mathrm{f} = [2\log_{10}\mathrm{Re} - 0.65]^{-2.3}, \qquad [18]$$

Having computed the skin friction coefficient, the wall shear stress is calculated as

$$\tau_\mathrm{w} = \frac{1}{2}\rho U_0^2 C_\mathrm{f}. \qquad [19]$$

The friction velocity, which can be commonly estimated with Eq. [15] only after performing a full RANS modeling, a priori can be computed using Eq. [19] for the wall shear stress:

$$u_\tau = \sqrt{\tau_\mathrm{w}/\rho}. \qquad [20]$$

Finally, the Eq. [14] for y^+ can be rearranged to give the centroid of the wall adjacent cell as

$$\Delta = \frac{\mu_\ell y^+}{\rho u_\tau}. \qquad [21]$$

Thus, the height of the first mesh layer becomes 2Δ by assuming regular hexahedral shape of the cells. An initial CFD analysis should be carried out with the corresponding assembled mesh and is followed by the reduction of the cell height according to the quality criteria.

It is recommended to avoid placing near-wall cell layer within the buffer region ($5 < y^+ < 30$) since the blending behavior, defined by the wall functions, is not precise in this range. That is also valid for the log-law interval ($y^+ > 30$), where the wall functions are likely to be inaccurate for expected flow separation regions or zones with severe pressure gradients it should.

Thereby, it is of a great advance to keep the wall adjacent cells inside a viscous sublayer ($y^+ < 5$) for the URANS modeling, which was approved in the presented study by verification against experimental measurements and observations. The mesh growth through the flow boundary layer can be estimated from its thickness δ_{99}, presented in a book by Çengel and Cimbala[34] for the laminar regime

$$\delta_{99} = 4.91 L_0/\sqrt{\mathrm{Re}}, \quad [22]$$

or by the alternative correlation for the developed turbulent flow as

$$\delta_{99} = 0.38 L_0/\mathrm{Re}^{1/5}. \quad [23]$$

Typically, the CFD engineers should aim between 5 and 30 inflation layers inside the boundary layer.

However, the DNS results, serving as an origin for the wall functions formulation, are typically obtained for an "ideal" case of the turbulent flow along the plate, as for example in Moser *et al.*[23] Hence, the conventional approach for the strong melt flow with adverse pressure gradients and flow separation inside the SEN, suggested here, is to obtain y^+ closer to 1. Moreover, the wall boundary layers must be further refined if that criterion is missed. Initial guess on the mesh quality can be additionally made using more robust standard k–ε RANS, using 2D simplification of the geometry or, as in the presented study, against the experimental measurements. The standard k–ε model can also be employed for the initial simulation iterations to avoid a drastic jump in a solution at the starting phase.

Monitoring turbulent variables for positive boundedness and avoiding their strong fluctuations is of great importance. The usage of the high-order upwind-blended advection schemes strongly assists for the turbulent closure equations together in combination with the gradient limiting to guaranty boundedness and suppress unphysical oscillations of the numerical solution.[49]

V. CONCLUSIONS

A water modeling of the flow inside a thin slab continuous caster was performed for a single port SEN with different gap sizes. The traditional meshing approach by keeping the y^+ in a reasonable range gave a good agreement for the URANS simulations of a classical double roll pattern in the experiment. At certain casting regime, single jet oscillations were experimentally detected, which could not be predicted numerically using similar modeling setup.

The studies were performed with an aim to (i) reveal the origins of the poor model performance; (ii) improve the modeling approach to fit the experiment; and (iii) establish the guidelines for the industrial application of the CFD simulation technique using URANS approach in CC.

The study revealed that wall mesh quality control is crucial especially to predict the flow detachment inside the SEN. The criterion of the wall adjacent cells in the viscous sublayer ($y^+ < 5$) is proposed and verified with the experimental data. The coarser mesh can be employed in the rest of the domain to maintain computational efficiency. A priory estimation of the wall mesh quality along the critical zones is described in detail.

The flow oscillation behavior of the formed single jet was predicted in the mold region by two sophisticated URANS approaches (RKE and k–ω SST). Both models gave strongly matching results. However, k–ω SST showed less diffusive behavior. A FFT analysis showed a slight overprediction of the main flow frequencies in the simulation and some under-estimation of the submeniscus velocity amplitude. The reason lays in the unresolved (by the URANS approach) turbulence structures, in excluding of the free surface from the numerical model, or/and due to the uncertainties in the experimental measurement. In further studies, the more sophisticated scale adaptive simulation (SAS) or large eddy simulation (LES) methods will be applied and investigated.

ACKNOWLEDGMENTS

The authors acknowledge financial support from the Austrian Federal Ministry of Economy, Family, and Youth and the National Foundation for Research, Technology, and Development within the framework of the Christian Doppler Laboratory for Metallurgical Applications of Magnetohydrodynamics. The water model experiment was performed at the RHI Magnesita GmbH Training Centre in Leoben (Austria).

CONFLICT OF INTEREST

On behalf of all authors, the corresponding author states that there is no conflict of interest.

FUNDING

Open access funding provided by Montanuniversität Leoben.

SUPPLEMENTARY INFORMATION

The online version contains supplementary material available at https://doi.org/10.1007/s11663-024-03002-8.

NOMENCLATURE

BC	Boundary condition
CC	Continuous casting
CD	Central-differencing discretization
CFD	Computational fluid dynamics
FFT	Fast Fourier transform
FVM	Finite volume method
RANS	Reynolds-averaged Navier–Stokes equations
RKE	Realizable k–ε RANS turbulence model
SST	Shear stress transport
UFM	Single port SEN design, produced by RHI Magnesita GmbH
URANS	Unsteady RANS
UW	Upwind discretization
SEN	Submerged entry nozzle
TSC	Thin slab casting
$C_{1\varepsilon}$,	Turbulence model constants
C_μ,$C_{2\varepsilon}$	Turbulence model parameters (velocity gradient dependent)
CFL	Courant–Friedrichs–Lewy condition
E	Wall function constant
G	Shear production of turbulence kinetic energy
H_i	FFT output values
$\mathrm{Pr}_{t,k}$	Turbulent Prandtl number for turbulent kinetic energy
$\mathrm{Pr}_{t,\varepsilon}$	Turbulent Prandtl number for turbulent kinetic energy
Re	Reynolds number
Q_m	Volumetric flow rate for the water model
Q_r	Volumetric flow rate for the real casting process
Y_i	Normalized FFT values
k	Turbulent kinetic energy
p	Pressure
t	Time
$\mathbf{u}$	Velocity
u_m	Casting speed in the water experiment
u_r	Casting speed of the real process
u_τ	Friction velocity at the wall
$\dot{\boldsymbol{\varepsilon}}$	Rate-of-strain tensor
ε	Turbulence dissipation rate
κ	Von Karman constant
μ_{eff}	Effective viscosity
μ_ℓ	Molecular dynamic viscosity
μ_t	Turbulent dynamic viscosity
ρ	Density
ω	Turbulence specific dissipation rate
Δ	Distance from the wall
y^+	Mesh y-plus factor
y^+_{lam}	y-Plus factor for the boundary of viscous/logarithmic sublayers

REFERENCES

1. C. Bernhard, H. Hiebler, and M.M. Wolf: *Ironmak. Steelmak. Steelmak.*, 2000, vol. 27, pp. 450–54.
2. B. Zhao, B.G. Thomas, S.P. Vanka, and R.J. O'Malley: *Metall. Mater. Trans. B*, 2005, vol. 36B, pp. 801–23.
3. A. Vakhrushev, M. Wu, A. Ludwig, Y. Tang, G. Hackl, and G. Nitzl: *Metall. Mater. Trans. B*, 2014, vol. 45B, pp. 1024–37.
4. P.D. Lee, P.E. Ramirez-Lopez, K.C. Mills, and B. Santillana: *Ironmak. Steelmak.*, 2012, vol. 39, pp. 244–53.
5. B.G. Thomas: in *Making, Shaping and Treating of Steel*, vol. 5, A. Cramb, ed., AISE Steel Foundation, Pittsburgh, PA, 2003, p. 14.1–41.
6. M.G. González-Solórzano, R.M. Dávila, J. Guarneros, I. Calderón-Ramos, C.R. Muñiz-Valdés, and A. Nájera-Bastida: *Fluids*, 2022, vol. 7, p. 288.
7. H. Barati, M. Wu, A. Kharicha, and A. Ludwig: *Powder Technol.*, 2018, vol. 329, pp. 181–98.
8. H. Barati, M. Wu, A. Kharicha, and A. Ludwig: *Steel Res. Int.*, 2020, vol. 91, p. 2000230.
9. H. Barati, M. Wu, S. Michelic, S. Ilie, A. Kharicha, A. Ludwig, and Y.-B. Kang: *Metall. Mater. Trans. B*, 2021, vol. 52B, pp. 4167–78.
10. A. Vakhrushev, A. Kharicha, M. Wu, A. Ludwig, Y. Tang, G. Hackl, G. Nitzl, J. Watzinger, and J. Bohacek: *Metals*, 2021, vol. 11, p. 1375.
11. H.G. Weller, G. Tabor, H. Jasak, and C. Fureby: *Comput. Phys.*, 1998, vol. 12, p. 620.
12. S. Pirker, D. Kahrimanovic, and S. Schneiderbauer: *Metall. Mater. Trans. B*, 2015, vol. 46B, pp. 953–60.
13. C. Kratzsch, K. Timmel, S. Eckert, and R. Schwarze: *Steel Res. Int.*, 2015, vol. 86, pp. 400–10.
14. C. Kratzsch, A. Asad, and R. Schwarze: *J. Manuf. Sci. Prod.*, 2015, vol. 15, pp. 49–57.
15. Z. Liu, A. Vakhrushev, M. Wu, A. Kharicha, A. Ludwig, and B. Li: *Metall. Mater. Trans. B*, 2019, vol. 50B, pp. 543–54.
16. M.G. González-Solórzano and R.D. Morales: *Steel Res. Int.*, 2022, vol. 93, p. 2200395.
17. K. Jin, S.P. Vanka, and B.G. Thomas: *Metall. Mater. Trans. B*, 2017, vol. 48B, pp. 162–78.
18. R. Vertnik, K. Mramor, and B. Šarler: *Eng. Anal. Bound. Elem.*, 2019, vol. 104, pp. 347–63.
19. K. Mramor, R. Vertnik, and B. Šarler: *IOP Conf. Ser.*, 2023, vol. 1281, p. 012029.
20. M. Wu, A. Vakhrushev, G. Nummer, C. Pfeiler, A. Kharicha, and A. Ludwig: *TOTPJ*, 2010, vol. 2, pp. 16–23.
21. M. Wu, A. Vakhrushev, A. Ludwig, and A. Kharicha: *IOP Conf. Ser.*, 2016, vol. 117, p. 012045.
22. J. Gregorc, A. Kunavar, and B. Šarler: *Metals*, 2021, vol. 11, p. 1140.
23. R.D. Moser, J. Kim, and N.N. Mansour: *Phys. Fluids*, 1999, vol. 11, pp. 943–45.
24. A. Vakhrushev, Menghuai Wu, A. Ludwig, Y. Tang, G. Nitzl, and G. Hackl: in *Proceedings of the 8th ECCC Conference*, On storage device, Graz, Austria, 2014, p. 10.
25. A. Vakhrushev, M. Wu, A. Ludwig, G. Nitzl, Y. Tang, G. Hackl, and R. Wincor: *Steel Res. Int.*, 2017, vol. 88, p. 1600276.
26. M. Javurek, M. Thumfart, and R. Wincor: *Steel Res. Int.*, 2010, vol. 81, pp. 668–74.
27. M. Thumfart, G. Hackl, and W. Fellner: *Steel Res. Int.*, 2022, vol. 93, p. 2100824.

28. R.D. Morales, Y. Tang, G. Nitzl, C. Eglsäeer, and G. Hackl: *ISIJ Int*., 2012, vol. 52, pp. 1607–15.
29. E. Torres-Alonso, R.D. Morales, J. Palafox-Ramos, and P. Ramírez-López: *Steel Res. Int*., 2008, vol. 79, pp. 553–63.
30. Y.J. Jeon, H.J. Sung, and S. Lee: *Metall. Mater. Trans. B*, 2010, vol. 41B, pp. 121–30.
31. Z. Liu, B. Li, and F. Tsukihashi: *ISIJ Int*., 2015, vol. 55, pp. 805–13.
32. S. Garcia-Hernandez, C.H. Gonzalez-Guzman, R. Morales Davila, J.J. Barreto, E. Gutierrez, and I. Calderon-Ramos: *Crystals*, 2020, vol. 10, p. 958.
33. A. Vakhrushev, A. Kharicha, E. Karimi-Sibaki, M. Wu, A. Ludwig, G. Nitzl, Y. Tang, G. Hackl, and J. Watzinger: *Steel Res. Int*., 2022, vol. 93, p. 2200088.
34. Y.A. Çengel and J.M. Cimbala: *Fluid Mechanics: Fundamentals and Applications*, 3rd ed. McGraw Hill, New York, 2014.
35. D. Mazumdar, M. Krshnavtar, R. Mishra, and P. Singh: in *The 8th International SteelSim Conference*, AIST, 2019, pp. 769–79.
36. M. Bielnicki and J. Jowsa: *Metall. Res. Technol*., 2020, vol. 117, p. 509.
37. T.-H. Shih, W.W. Liou, A. Shabbir, Z. Yang, and J. Zhu: *Comput. Fluids*, 1995, vol. 24, pp. 227–38.
38. F.R. Menter: *AIAA J*., 1994, vol. 32, pp. 1598–1605.
39. F.R. Menter, M. Kuntz, and R. Langtry: in *Turbulence, Heat, and Mass Transfer 4*, Begell House, Antalya, Turkey, 2003, pp. 625–32.
40. J.H. Ferziger and M. Perić: *Computational Methods for Fluid Dynamics*, 3rd, rev ed. Springer, Berlin, 2002.
41. C.M. Rhie and W.L. Chow: *AIAA J*., 1983, vol. 21, pp. 1525–32.
42. C. Greenshields: *OpenFOAM v8 User Guide*, The OpenFOAM Foundation, London, 2020.
43. S.V. Patankar: *Numerical Heat Transfer and Fluid Flow*, Hemisphere Pub. Corp., McGraw-Hill, Washington, 1980.
44. R.I. Issa: *J. Comput. Phys*., 1986, vol. 62, pp. 40–65.
45. B.E. Launder and D.B. Spalding: *Comput. Methods Appl. Mech. Eng*., 1974, vol. 3, pp. 269–89.
46. H. Schlichting (Deceased) and K. Gersten: *Boundary-Layer Theory*, 9th ed. 2017., Springer Berlin Heidelberg: Imprint: Springer, Berlin, 2017.
47. D.C. Wilcox: *Turbulence Modeling for CFD*, 3rd ed. DCW Industries, La Cãnada, CA, 2006.
48. P. Duhamel and M. Vetterli: *Signal Process*., 1990, vol. 19, pp. 259–99.
49. G.N. Barakos, P. Doerffer, and M.M. Luczak, eds.: *Recent Progress in Flow Control for Practical Flows: Results of the STADY-WICO and IMESCON Projects*, 1st ed. 2017., Springer International Publishing: Imprint: Springer, Cham, 2017.